1 **Title page**
2
3 **Title:**
4 Transverse and axial resolution of femtosecond laser ablation
5
6 **Running title:**
7 Axial resolution of laser ablation
8
9 **Author names and affiliations:**
10 Yao L. Wang[1◊], Noa W. F. Grooms[1◊], Samuel H. Chung[1*]
11 [◊]equal contribution
12 [1]Department of Bioengineering, Northeastern University, Boston, Massachusetts, USA
13
14 *Corresponding author
15 E-mail: schung@northeastern.edu
16

17 **Keywords:** pulsed laser, femtosecond laser, laser ablation, laser surgery, transverse
18 resolution, axial resolution, *Caenorhabditis elegans*, regeneration
19
20 **Author contributions:**
21 Several people contributed to the work described in this paper. SHC conceived the idea.
22 YLW and NWFG carried out experiments, and all authors analyzed the data. SHC
23 supervised the experiments and the development of the manuscript. SHC wrote the first
24 draft of the manuscript; all authors subsequently took part in the revision process and
25 approve the final copy of the manuscript.

26 **Abstract**

27 Femtosecond lasers are capable of precise ablation that produce surgical dissections *in*

28 *vivo*. The transverse and axial resolution of the laser damage inside the bulk are

29 important parameters of ablation. The transverse resolution is routinely quantified, but

30 the axial resolution is more difficult to measure and is less commonly performed. In

31 some *in vivo* samples, fine dissections can also be difficult to visualize, but *in vitro*

32 samples may allow clear imaging. Using a 1040-nm, 400-fs pulsed laser, we performed

33 ablation inside agarose and glass, producing clear and persistent damage spots. Near

34 the ablation threshold of both media, we found that the axial resolution is similar to the

35 transverse resolution. We also ablated neuron cell bodies and fibers in *C. elegans* and

36 demonstrate submicrometer resolution in both the transverse and axial directions,

37 consistent with our results in agarose and glass. Using simple yet rigorous methods, we

38 define the resolution of laser ablation in transparent media along all directions.

Introduction

The advent of the laser in 1960[1] was rapidly followed by its application for ablation in a variety of research and medical samples (reviewed in Ref. [2]). Scientists and clinicians recognized that focused laser light can produce highly confined damage to materials, resulting in dissection with resolution unachievable through conventional means. In plasma-mediated laser ablation, the sample absorbs sufficient energy from laser light to vaporize the material[3]. When this absorption occurs on a surface, material is explosively removed. Ablation in the bulk requires laser light to penetrate through the sample to its target. To permit propagation of any appreciable distance, the sample must be relatively transparent to the laser wavelength. Absorption of laser light in the bulk is typically achieved by focusing the laser beam and thereby stimulating nonlinear absorption[4,5]. Depending on the amount of laser energy deposited, the laser generates plasma of various densities, leading to localized damage at the focal volume. At energies significantly above the vaporization energy of the media, an explosion and shockwaves can generate damage beyond the focal volume[6,7].

The foundational studies on plasma-mediated ablation of water apply to laser ablation of biological media, as they are primarily composed of water. The mechanisms of laser propagation and nonlinear absorption are also similar between many transparent materials. Thus, studies performed on various glasses and transparent semiconductors may be relevant to understanding the processes of laser ablation on biological media. Based on prior studies in ablation of transparent material, key parameters for laser ablation include the intensity thresholds for nonlinear absorption and for ablation. An intensity above the absorption threshold produces strong nonlinear

62 absorption, and energy transfers into the material[4]. Together with the parameters for

63 laser focusing, the ablation threshold sets a focal volume where the laser pulses can

64 vaporize material and create damage.

65   While assessing the transverse resolution of a laser ablation technique is very

66 common, significantly fewer studies assess the axial, or longitudinal, resolution of

67 ablation. This is partially due to the practical challenges of imaging along the optical

68 axis: laser ablation is often paired with widefield imaging of directions orthogonal to the

69 optical axis. Prior studies have gained optical access to side-views through several

70 methods: In one study, an ablated piece of glass was polished down to access the

71 damage spot[8]. Other studies fractured the glass and then imaged it with brightfield,

72 differential interference contrast microscopy, or scanning electron microscopy following

73 graphite coating[9,10]. Another study used two objectives to image from the side while

74 ablating[11], and a recent study physically cut a soft sample with a razor blade to expose

75 the damaged spot[12].

76   A steadily growing number of studies have characterized laser ablation of biological

77 samples (*e.g.*, Refs. [13,14]). Our laboratory studies neurons in the nematode *C.*

78 *elegans*, in part utilizing femtosecond laser ablation. Given the importance of ablation

79 (and imaging) resolution in the axial direction, we seek to establish rigorous techniques

80 for assessing it. In prior studies we established a technique to measure the illumination

81 resolution of widefield and scanned microscopy[15], and demonstrated submicrometer

82 transverse resolution of ablation with a similar femtosecond laser[14]. Here, we first

83 measure both the transverse and axial resolution of laser ablation in agarose and glass,

84 materials with permanent visible damage. We find that the transverse and axial

85   diameters of the minimum damage spot are very similar, in both materials. The size of

86   the damage spot over different laser powers obey a simple model of propagation and

87   absorption, from which we can calculate the threshold intensity and the minimum focal

88   spot size[16]. Second, we establish an upper bound on the damage sizes in the

89   transverse and axial directions to define the resolution in *C. elegans in vivo*. Third, we

90   present evidence suggesting that neuron fibers are not damaged by laser irradiation

91   outside of the axial damage region.

92

Results

94   Our setup is shown in Fig. 1a, and a similar setup was described in detail[13]. Various

95   optics and laser parameters impact the laser ablation resolution, including laser

96   wavelength, pulse duration, pulse energy, exposure time, repetition rate, and the

97   numerical aperture (NA) of the microscope objective. In our experiments, most of these

98   parameters are fixed. A femtosecond laser outputs 1040-nm 400-fs pulses at 1 kHz,

99   which we expand and send into a 1.4 NA, 60x objective. In our biological samples, we

100   image epifluorescently through the same objective. We input illumination light into the

101   sample, and we image fluorescent light from the sample onto an array camera.
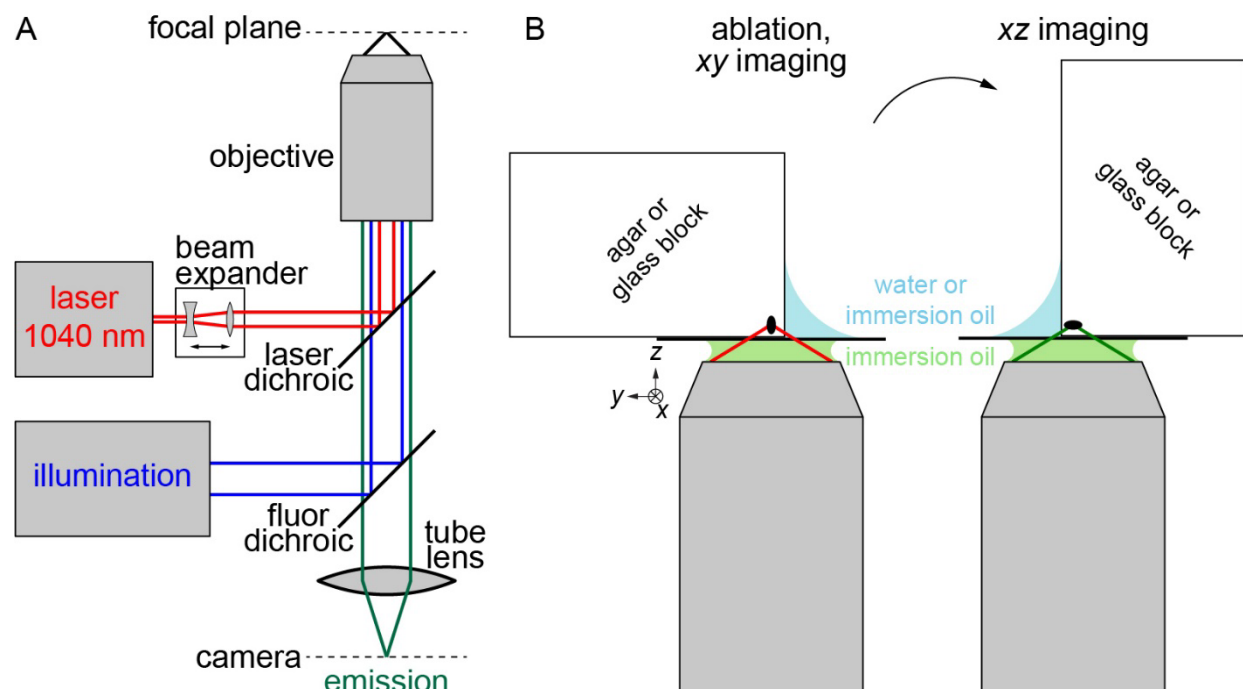
102

Fig 1. Ablation and imaging setup. (A) Microscope setup for ablation and imaging. 1040-nm femtosecond laser beam is expanded and focused on sample by objective. Illumination light is focused by same objective, and emission light is imaged onto array camera by tube lens. (B) Setup for ablation and imaging. Transverse (*xy*) imaging in same configuration as ablation. Axial (*xz*) plane imaging by ablating block near edge, rotating block 90°, and imaging. Gaps in beampath are filled with water and/or immersion oil to homogenize refractive index.

Theoretical considerations in a simplified ablation model

This section derives the transverse (*xy*) and axial (*z*) intensity distributions for a focused beam propagating in the *z* direction in a homogeneous medium. We partially follow the derivation in Chapter 2.5 of Ref. [17] with adjustments to follow the derivation in Ref. [16]. We utilize the final results in the following sections to model the ablation we

117   observe and determine the ablation parameters, similar to our prior work that was

118   limited to the transverse direction[14].

119   We model focused laser beams with a Gaussian intensity distribution in the

120   transverse direction. Because of diffraction, focused beams come to a minimum width

121   called the waist, at the focal plane (see S1A Fig). The beam width is hyperboloid in the

122   axial direction, and the corresponding intensity distribution is Lorentzian (see S1B Fig).

123   In our simplified model, the laser pulses propagate without scattering, absorption, or

124   nonlinear effects. When the local laser intensity exceeds the intensity threshold for

125   nonlinear absorption, laser energy is deposited into the media. The absorption of

126   sufficient energy generates plasma that vaporizes the material (plasma-mediated

127   ablation). Under our model, ablation occurs when the laser intensity exceeds an

128   threshold for ablation, following similar work examining phase transitions in silicon[16]. In

129   our experience, this simplified model explains many of the key characteristics of the

130   ablation we note in our experiments on transparent materials near the ablation

131   threshold. We remark on the limitations of the model in the discussion.

132   The local laser intensity is $I(x,y,z) = P / A = P / \pi r^2$, where I, P, A, and r are the

133   optical intensity, optical power, beam cross-sectional area, and beam radius,

134   respectively. Specifically,

$$I(x, y, z) = \frac{P_0}{\pi \omega^2(z)} e^{-\frac{x^2+y^2}{\omega^2(z)}}.$$

135   where P_0 is the peak power level and $\omega^2(z) = \omega_0^2 \left[1 + \frac{z^2}{z_0^2}\right]$ is the squared radius of the

136   beam. ω_0 is the beam waist radius at $1/e^2$ of the maximum intensity. z_0 is the Rayleigh

137   range, or the axial distance from the waist where the intensity drops by half[17], and 2 z_0

138   is also known as the confocal parameter. Intuitively, the total power at each axial

139   position must be constant if there is no absorption or scattering. Confirming this, the

140   total power is the integral of *I(x,y,z)* over the transverse directions, which yields the peak

141   power, P_0.

142

143   We consider simple beams with azimuthal symmetry, so $r^2 = x^2 + y^2$ and

$$I(r,z) = \frac{P_0}{\pi \omega^2(z)} e^{-\frac{r^2}{\omega^2(z)}}.$$

144   Thus, at the waist ($z = 0$) the intensity is

$$I(r,0) = \frac{P_0}{\pi \omega_0^2} e^{-\frac{r^2}{\omega_0^2}}.$$

145   Along the optical axis ($r = 0$) the intensity is

$$I(0,z) = \frac{P_0}{\pi \omega^2(z)} = \frac{P_0}{\pi \omega_0^2} \frac{1}{1 + z^2/z_0^2}.$$

146   Absorption of laser beams in nominally transparent materials occurs if the laser intensity

147   exceeds a threshold, I_{th}, dependent on the optical properties of the material[4]. The laser

148   intensity distribution is peaked in the transverse and axial directions. For a given laser

149   power, the intensity meets the threshold at defined transverse r_{th} or axial z_{th} radii, where

150

$$I(r_{th},0) = \frac{P_0}{\pi \omega_0^2} e^{-\frac{r_{th}^2}{\omega_0^2}} = I_{th}$$

151   or

$$I(0,z_{th}) = \frac{P_0}{\pi \omega_0^2} \frac{1}{1 + z_{th}^2/z_0^2} = I_{th}.$$

152   Within this r_{th} or z_{th}, laser energy is deposited and material can be ablated, forming a

153   damage spot. The pulse energy, E, is the time integral of $P(t)$, the time evolution of a

154   single pulse's power. Assuming a Gaussian shape in time, $P_0 = \sqrt{\frac{4\ln 2}{\pi}}\,E/\tau = 0.94\,E/\tau$,

155   where τ = 400 fs is the pulse duration[18]. The average laser power is $P_{avg} = E * f_{rep}$,

156   where f_{rep} = 1 kHz is the repetition rate. Thus, the respective radii of the damage spot in

157   the transverse and axial directions are

158    $$r_{th}\left(P_{avg}\right) = \omega_0 \sqrt{\ln\frac{P_0}{\pi\omega_0^2 I_{th}}} = \omega_0 \sqrt{\ln\frac{0.94\,P_{avg}}{\tau f_{rep}\pi\omega_0^2 I_{th}}}$$ Eq. 1

159   and

160    $$z_{th}\left(P_{avg}\right) = z_0 \sqrt{\frac{P_0}{\pi\omega_0^2 I_{th}} - 1} = z_0 \sqrt{\frac{0.94\,P_{avg}}{\tau f_{rep}\pi\omega_0^2 I_{th}} - 1}.$$ Eq. 2

161

162   Agarose and glass ablation

163   The resolution of laser ablation *in vivo* can be difficult to assess. The media itself is

164   often heterogeneous, complicating observation of laser-induced structural changes.

165   Following ablation of soft tissue, damage locations rapidly flood with water from

166   surrounding regions, which reduces index differences and contrast between the

167   damage spot and the background. We sought to find a biological medium with

168   permanent index changes following ablation to allow precise measurement of damage

169   sizes. We found that ablated agarose has a persistent, albeit small, index change (see

170   Fig. 2ac). Ablation studies have utilized agarose as a proxy for soft tissues due to their

171   similar mechanical and thermal properties[19,20]. For instance, *C. elegans* has a Young's

172   modulus around 50 kPa, similar to that of agarose gels[21]. The primary component of

173   both agarose and transparent soft tissues is water, and these media have similar

174   refractive indices. The refractive indices of water, 4% agarose, and *C. elegans* tissue

175   are 1.333, 1.339, and 1.379, respectively[22,23]. Because of their similar refractive index,

176   we expect the propagation of light through agarose and *C. elegans* tissue to be similar.

177   While the resolution and threshold of laser ablation in *C. elegans in vivo* is different from

178   agarose, the agarose ablations provide information on the relative size of the axial

179   resolution compared to the transverse resolution.
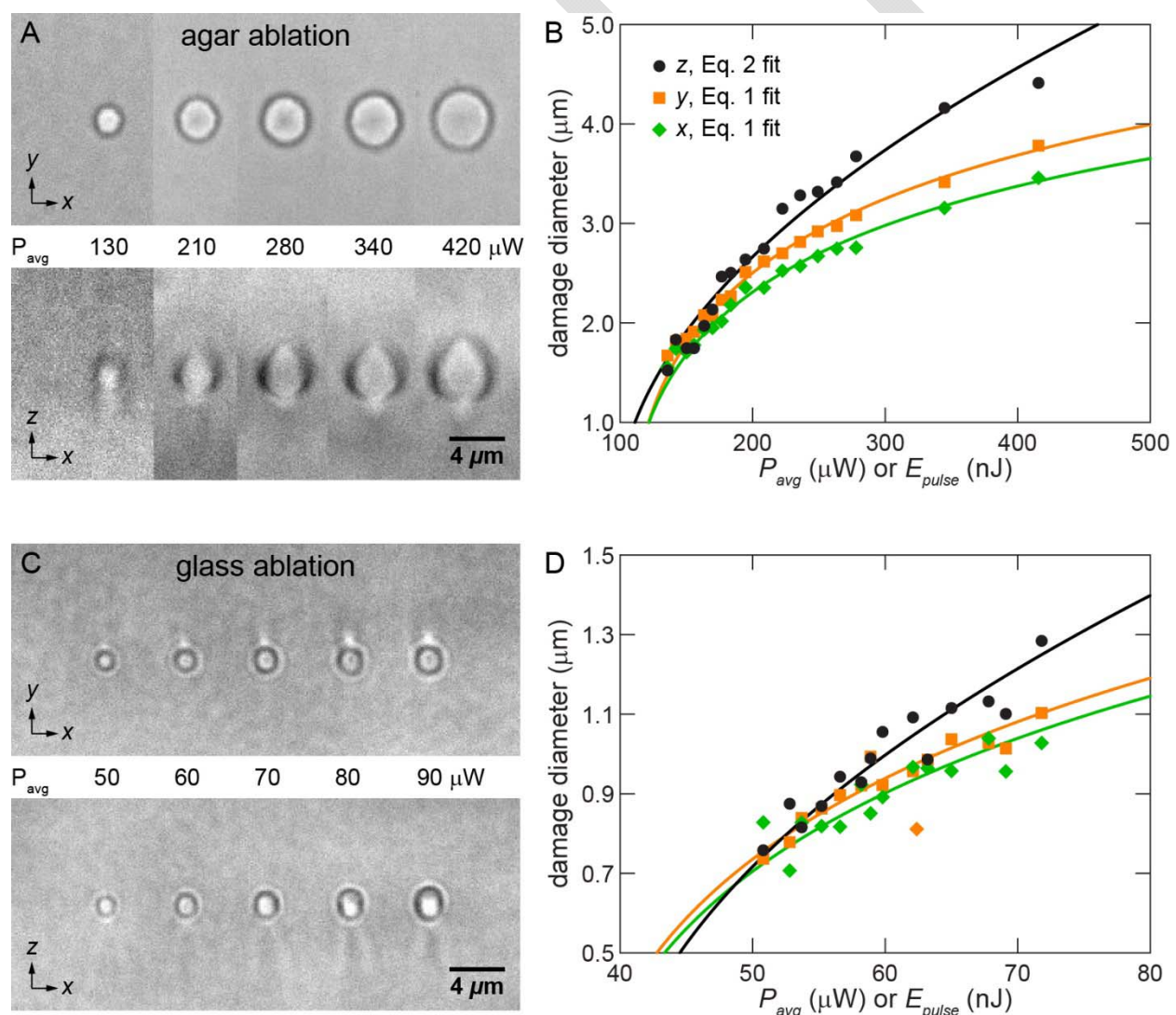
180

181

182 **Fig 2. Glass damage spots match theoretical predictions.** (A) Transverse and axial

183 plane images of agarose ablation by focused laser pulses. (B) Ablation spot

184 measurements in *x* (diamond), *y* (square), and *z* (circle) directions. Green and orange

185 curves plot Eq. 1 with best fit ω_0 and I_{th}. Black curve plots Eq. 2 with best fit z_0 and I_{th}.

186 (C) Images of glass ablation. (D) Ablation spot measurements in *x*, *y*, and *z* directions,

187 with best fit curves.

188

189   Measuring transverse sizes of the damage spot at various pulse energies is

190 relatively straightforward as ablation and reimaging can occur under the same

191 configuration. Measuring the axial size of the damage spot is significantly more difficult.

192 As shown in Fig. 1b, after ablating a block of agarose near a corner, we rotated the

193 block 90° to image the damage spot in the orthogonal (*i.e.*, *xz*) direction. We fill spaces

194 between the coverslip and the agarose block with water (blue). The water minimizes

195 changes in refractive index for the portions of the ablation and imaging beams that do

196 not enter the agarose block directly from the coverslip. This homogenization maximizes

197 light transmission and minimizes optical distortion.

198   We ablated agarose with 100-400 μW average power, producing damage spots of

199 various diameters in *x*, *y*, and *z* (see Fig. 2a). We empirically determined that the

200 agarose damage threshold under our setup is 120 μW average power at 1 kHz

201 repetition rate, or 120 nJ pulse energy. Surprisingly, near the ablation threshold the spot

202 diameters in transverse and axial directions were very similar, producing a roughly

203 spherical damage spot. In the section above, we derive the equations governing the

204 intensity distribution in the transverse (Gaussian) and axial (Lorentzian) directions. As

—11—

205   the pulse energy increased, the axial diameter of the damage spot increased more

206   rapidly than the transverse, as expected from Eqs. 1-2. Fitting the transverse agarose

207   damage spot measurements to Eq. 1, we obtain transverse waist radii ω_0 in the x and y

208   directions of 1.5 and 1.6 μm, and an ablation intensity thresholds of I_{th} = 3.7 and 3.1 ×

209   10^{12} W/cm^2 for ablation of agarose (see Fig. 2b, Tab. 1). We believe the waist radius in

210   the y direction is larger than x direction because some of the beam in the y direction

211   passes through a section of water (see Fig. 1b), which has a slightly different refractive

212   index than agarose. Fitting the axial damage spot measurements to Eq. 2, we obtain an

213   axial radius z_0 = 1.3 μm and a separate ablation intensity threshold I_{th} = 3.3 × 10^{12}

214   W/cm^2 (see Fig. 2b, Tab. 1). The calculated transverse and axial waist diameters are

215   similar, which is confirmed by roughly spherical damage spots near the threshold.

216   We obtained similar results with the same trends by ablating a thin cylinder of

217   agarose in a water-filled channel (data not shown). Compared to the agarose block, the

218   ablation resolution in the cylinder was not as fine and the imaging was not as clear. We

219   speculate that this is due to refraction from the curvature of the cylinder and increased

220   depth of ablation and imaging. We did not pursue ablations in this configuration further.

221

222   **Table 1: Ablation parameters**

	Agarose ablation			Glass ablation		
	x	*y*	*z*	*x*	*y*	*z*
ω_0 (μm)	1.5	1.6		0.66	0.68	
z_0 (μm)			1.3			0.69
I_{th} (W/cm^2)	3.7 × 10^{12}	3.1 × 10^{12}	3.3 × 10^{12}	6.5 × 10^{12}	6.0 × 10^{12}	6.5 × 10^{12}

223

224   We carried out ablations in N-BK7 glass to confirm the similarity between the axial

225   and transverse resolution that we observed in agarose. Ablation of glass leads to a

226   permanent and distinct change in the refractive index that allows a more precise

227   measurement of the damage spot than is possible in agarose. We also ablate glass with

228   power levels that are closer to levels used in ablations of *in vivo* samples. We followed a

229   similar procedure to the agarose ablations above but used immersion oil around the

230   block (see Fig. 1b). We ablated glass with 50-90 μW (see Fig. 2b) and found that the

231   ablation threshold is 50 μW average power, or 50 nJ pulse energy. Results from

232   ablation of glass confirmed the overall pattern of results in agarose (see Fig. 2b, Tab.

233   1). Transverse and axial sizes of damage spots near the threshold were very similar

234   and the smallest spots appeared spherical. The calculated waist radii ω_0 and confocal

235   parameter z_0 were also similar. The ablation intensity threshold was about $I_{th} = 6.4 \times$

236   10^{12} W/cm^2.

237

238   *In vivo* ablation

239   We also characterized the transverse and axial resolution of our surgeries *in vivo* on

240   neurons in *C. elegans*. Following our prior studies[13,14], we first assessed transverse

241   resolution by ablating the middle dendrite in a tight bundle of dendrites. We ascertained

242   true ablation rather than photobleaching as the diffusible green fluorescent protein

243   (GFP) label does not return to the ablated region following irradiation[13]. The first

244   ablation in Fig. 3a (after #1) shows a cut of resolution better than 1.03 μm. The second

245   ablation (after #2) shows a cut of resolution better than 0.75 µm. The first cut widens

246   between the "after #1" and the "after #2" images due to dendrite tension, further

247   confirming a complete cut. These data indicate an *in vivo* transverse resolution of well

248   below 1 µm, a similar resolution to our prior work using 800-nm Ti:sapphire and 1030-

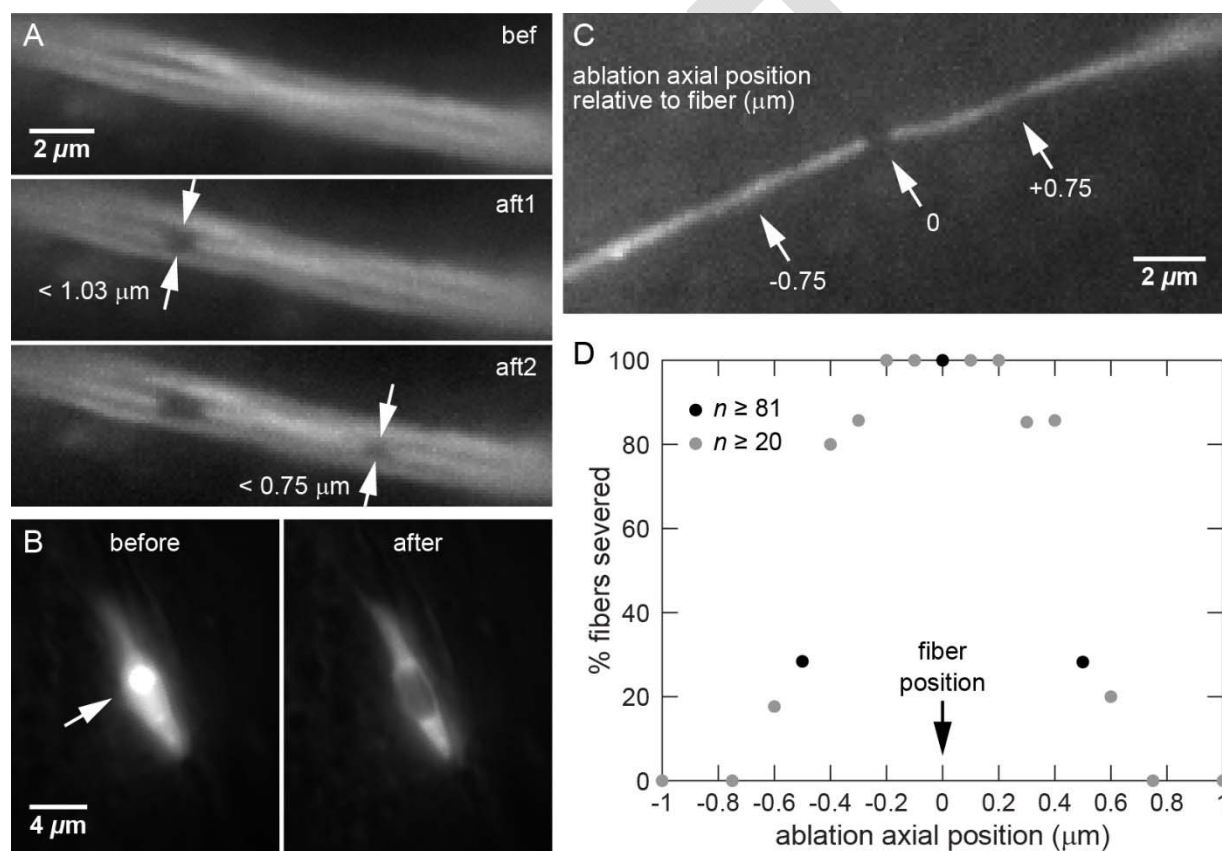249   nm Yb-doped fiber lasers[13,14].

250

252   **Fig 3. Characterization of *in vivo* laser ablation.** (A) Individual neuronal fibers in tight

253   bundle before, after 1st ablation, after 2nd ablation. Images indicate submicrometer

254   transverse resolution of laser ablation. (B) Ablation of nucleosol but not cytosol shows

255   persistence of nuclear membrane, suggesting axial resolution well below 2 µm. "After"

256   image taken immediately after ablation. (C) Fiber severed by ablation directly at its axial

—14—

257   position but spared by ablation 0.75 μm above or below fiber. (D) Percentage of fibers

258   severed by ablation at various axial positions relative to the fiber. Results indicate

259   submicrometer axial resolution of laser ablation.

260

261   Second, in multiple studies, we have ablated cell bodies for several seconds to kill

262   off entire cells[13,24]. We visualize and target single cells by a diffusible but cell-specific

263   GFP label. GFP diffusion through the fluid cell cytosol and nucleosol is very rapid, but

264   its diffusion across membranes in *C. elegans* neurons is much slower, on the order of

265   tens of seconds. In the early stages of cell body ablation, we often find that the nucleus

266   dims while the cytosol remains fluorescent (see Fig. 3b). This dimming occurs because

267   the interior of the nucleus is ablated while the nuclear membrane is spared. GFP from

268   throughout the nucleosol diffuses to the laser focus and is selectively ablated,

269   decreasing the fluorescence of the entire nucleus. The intact nuclear membrane greatly

270   slows the diffusion of cytoplasmic GFP into the nucleus and preserves the fluorescence

271   of the cytosol. As shown in Fig. 3b, irradiating the bright nucleolus (arrow) leads to

272   dimming of the entire nucleus but not the cell cytosol, confirming that ablation does not

273   damage the nuclear membrane. Thus, the axial resolution of laser ablation is far below

274   2 μm, the axial depth of the round nucleus.

275   Third, to further define the axial resolution, we focused laser pulses at specific

276   locations below, directly on, or above single neuronal fibers. As shown in Fig. 3c,

277   ablating at the fiber's axial position severs the fiber while ablating a sufficient distance

278   above or below the fiber does not sever the fiber. We tracked the percentage of fibers

279   severed by focusing at each depth relative to the fiber's axial position. As shown in Fig.

280 3d, the efficacy of laser ablation peaks when the laser pulses are focused on or near (≤

281 0.2 µm) the fiber. Surgical efficacy decreases roughly symmetrically as the focus moves

282 away from the fiber axially. At approximately ± 0.4-0.5 µm there is a clear transition from

283 severing to non-severing. Laser pulses focused at 0.75 µm away from the fiber or

284 further are unable to sever the fiber. There is noticeable pulse-to-pulse variability in the

285 laser's operation, producing a non-binary distribution. Sequential pulses can focus on

286 slightly different transverse and axial positions over a range of ~0.1-0.2 µm. Thus, these

287 data indicate that the axial resolution of laser ablation is slightly below 1 µm.

288   Lastly, we cut neurites in the ASJ neuron and noted axon regeneration after ablation

289 to provide another demonstration of surgical resolution. As shown in Fig. 4a, the ASJ

290 neuron consists of a cell body (light gray), dendrite (black), and axon (dark gray). In

291 mutant animals with defective dual-leucine zipper kinase, denoted as *dlk-1*, multiple

292 neuron types have severely reduced axon regeneration[25]. The ASJ axon shows no

293 regeneration in *dlk-1* animals when it is the sole fiber cut; however, nearly 100% of ASJ

294 axons regenerate when the ipsilateral sensory dendrite is severed concomitantly[26]. In

295 *dlk-1* animals, we cut the ASJ axon by ablating directly on the axon and then

296 immediately ablated at various depths relative to the dendrite. As shown in Fig. 4b, *dlk-1*

297 animals with axon cuts but no dendrite ablation showed no regeneration, confirming

298 prior results. When we cut axons and ablate directly on the dendrite, 95 ± 5% of

299 neurons regenerate. When the dendrite is ablated 0.5 µm above or below its depth

300 without severing it, there is minimal regeneration. These data further confirm the tight

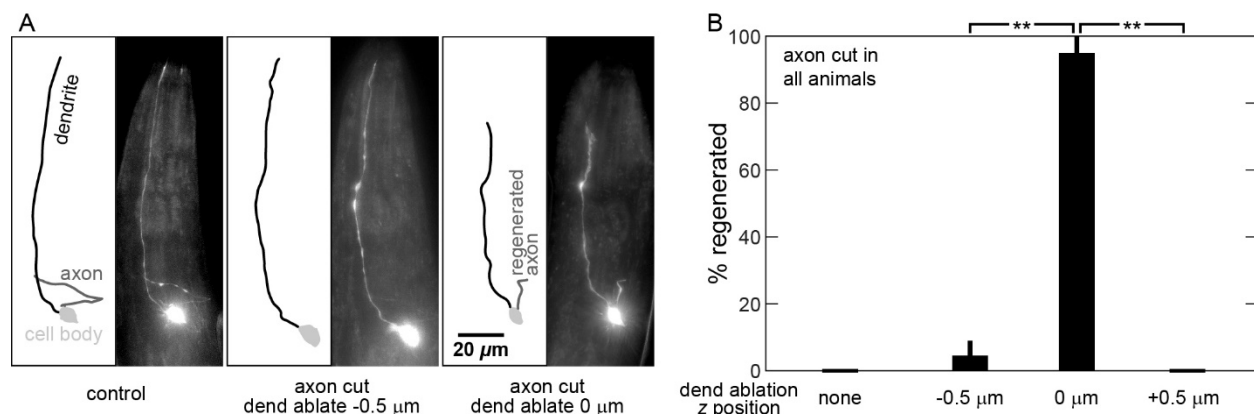301 confinement of laser damage to the focal plane.

302

303

Fig 4. Regeneration assay confirms submicrometer resolution of laser ablation.
(A) Line drawings and fluorescent images of ASJ neuron. Control (left) neuron with cell body (light gray), intact dendrite (black), and intact axon (dark gray). Non-control images taken 48 hours after ablation: Postablation neuron (middle) with cut axon and ablation 0.5 μm below dendrite. Axon has decayed away. Postablation neuron (right) with regenerated axon and dendrite ablated directly at its axial position. (B) Percentage of neurons regenerating following axon cut only (none) or axon cut with dendrite ablation at various depths. Significant regeneration only occurs when dendrites are ablated directly at their axial position. All animals are *dlk-1* mutants with axons cut. Average and standard deviation indicated by bars. ** $p < 0.0001$.

Discussion

While both the transverse and axial resolution are needed to fully characterize laser ablation, the axial resolution is rarely measured. Here we determine the transverse and axial resolution of a Yb-doped diode-pumped solid-state femtosecond laser by ablating

319 transparent materials and *in vivo* biological samples. By solving the Gaussian and

320 Lorentzian intensity distributions for r_{th} and z_{th}, we find that the transverse diameter of

321 ablation is proportional to the square root of the logarithm of P_{avg}, while the axial

322 diameter of ablation is proportional to the square root of P_{avg}. By ablating agarose and

323 glass at various powers, directly measuring the damage spot in all three dimensions,

324 and fitting the measurements to the equations derived, we find an intensity threshold of

325 3.4×10^{12} W/cm^2 for agarose ablation and 6.4×10^{12} W/cm^2 for glass ablation. Fitting

326 our transverse and axial data led to similar results in all three dimensions for damage

327 size and ablation threshold. Our results on glass are roughly consistent with prior

328 studies showing intensity thresholds of $8 - 20 \times 10^{12}$ W/cm^2 of various glasses under

329 femtosecond pulses of different wavelengths and pulse durations (*e.g.*, Refs. [27,28]).

330 Importantly, we demonstrate, in agarose and in glass, that the transverse and axial

331 resolution of laser ablation near the ablation threshold are very similar to each other

332 (see Fig. 2bd).

333   Our measurements of laser ablation spots in transparent materials obey our model

334 remarkably well, despite our model's simplified approach. Clearly, there are many other

335 effects involved in femtosecond laser propagation, absorption, and ablation: First, there

336 are several nonlinear propagation effects, including self-phase modulation, self-

337 focusing, and self-steepening[29]. We believe these effects are minimal because tight

338 focusing conditions minimizes the distance over which these nonlinear effects

339 accumulate. However, we note that we have not precompensated (*i.e.*, prechirped) for

340 chromatic dispersion of the beam as it travels from the laser to our sample. By

341 precompensating, it may be possible to reduce the energy needed to achieve the

—18—

342 ablation threshold, which could improve ablation resolution. Second, there is likely a

343 small amount of scattering or linear absorption throughout the beam, as deeper targets

344 require more power to ablate. Moreover, the threshold condition for nonlinear absorption

345 is an approximation for determining where absorption occurs. In reality, the absorption

346 is proportional to the intensity raised to the order of the nonlinear absorption process[4].

347 Third, the absorption mechanisms that generate plasma are much more complicated

348 than the simple nonlinear absorption and photoionization of our model. In fact,

349 avalanche ionization is the mechanism that absorbs the most laser light[6]. However,

350 nonlinear absorption dictates where the absorption occurs and thus the spatial extent of

351 the plasma-mediated damage. Finally, laser repetition rate impacts damage

352 mechanisms, particularly at higher rates, when laser pulses deposit energy faster than it

353 can diffuse away as heat, leading to cumulative thermal damage. Our laser operates

354 well below the 1 MHz repetition rate boundary for cumulative damage[30,31]. Even so, we

355 have seen some cumulative damage in agarose at power levels above those in Fig. 2b,

356 as evidenced by divergence between single pulse and multi-pulse ablation (data not

357 shown).

358 We also characterized the resolution of 1040-nm femtosecond laser ablation in *C.*

359 *elegans* neurons *in vivo*. Similar to our prior studies utilizing 800-nm pulses[13], we show

360 a transverse resolution that is submicrometer by ablation of tight fiber bundles.

361 Likewise, we show an axial resolution that is also submicrometer by observing the

362 frequency of successful severing and surgical impact on regeneration. Note that even

363 though the laser pulses pass through the neuronal fibers (Fig. 3c), the fibers are not

364 damaged unless the region where the laser intensity exceeds the threshold impinges on

365   the fiber. It is only in this region that laser light is absorbed and damage occurs.

366   Fundamentally, it is this nonlinear absorption that confines axial damage so tightly to the

367   focal volume and ultimately produces the high axial resolution.

368   An increasing number of studies utilize laser ablation in biological contexts. Laser

369   ablation allows selective submicrometer-resolution damage in the bulk at a user-defined

370   timepoint, which is unachievable by conventional methods such as genetics,

371   pharmacology, or manual dissection. Rigorously defining ablation resolution in all three

372   dimensions is crucial for understanding its capacity to produce highly precise

373   dissections without collateral damage. To our knowledge, our study is one of relatively

374   few studies that examine the axial resolution of plasma-mediated laser ablation in

375   transparent media or biological samples. In our *in vivo* experiments, defining the axial

376   resolution is all the more important because the epifluorescence imaging that guides

377   laser ablation has lower resolution in the axial than transverse directions. Ascertaining

378   that the resolution of laser ablation is similar in all three dimensions ensures high quality

379   dissections that are independent of the sample orientation.

Materials and methods

Microscope setup: We utilized a Nikon Ti2-E inverted microscope with a SOLA SE II LED light engine to take 3D image stacks. We used a 1.4 NA, 60x oil-immersion objective for ablation and imaging. This objective is designed for use with a #1.5 glass coverslip.

Laser setup: A Yb-doped diode-pumped solid-state laser (SpectraPhysics Spirit-1040-4W) outputs 1040-nm 400-fs pulses with a repetition rate of 1 kHz. As shown in Fig. 1a, we expanded the diameter of the laser beam through a 10x beam expander (Thorlabs GBE10-B) to overfill the back aperture of our microscope objective. We raised the beam using a custom periscope (not shown) to send into the upper turret of our epifluorescence inverted microscope. A mechanical shutter in the upper turret controls the laser irradiation. We illuminated with blue light for imaging through the lower turret, and the emission light was imaged by an sCMOS camera (Andor Zyla 4.2).

Agar ablation and imaging: Our ablation and imaging setup is shown in Fig. 1b. We utilized a 4% agarose block (Fisher BioReagents BP160-500). To fabricate the block, we poured molten 4% agarose solution into an open box made from glass slides. After solidifying, we cut the block and immediately immersed it in water to prevent its sharp edge from drying out and deforming. We placed this block onto a coverslip typically used for imaging with our objective. We added pure water to all locations that transmit the laser beam or illumination light. This water prevents impinging of illumination or laser light on a low-index region of air that could lead to refraction or reflection rather than transmission. We ablated agarose 40 µm below the surface with a 0.2 s exposure time. We acquired the damage spot *xy* images by brightfield imaging through the same

403   face as laser transmission. For *xz* imaging of the laser damage spot, we separated the

404   agarose block from the coverslip after ablation, rotated it by 90°, and repeated the same

405   process of attaching the coverslip and imaging on the orthogonal face.

406   **Glass ablation and imaging:** The glass ablation procedure (see Fig. 1b) was very

407   similar to the agarose ablation procedure with the following alterations: We performed

408   all glass ablation on an N-BK7 block of glass polished to 20-10 scratch-dig. We added

409   immersion oil to all the locations that transmit the laser beam or illumination light. We

410   carried out ablation and imaging with procedures similar to the agarose imaging above.

411   **Damage spot characterization:** Ablation of agarose or glass creates a damage spot

412   that refracts light in brightfield images. At the focal plane, the interior of the spot is

413   bright. In Fiji/ImageJ (https://imagej.net/software/fiji/), we measured the size of a

414   damage spot using the intensity profile of a line through the center of the spot. We

415   defined the size to be the inner diameter of the spot, where the intensity profile

416   intersects the background value. We utilized these sizes together with the average laser

417   power to fit Eqs. 1-2 and determine the minimum spot ω_0, z_0, and the intensity threshold

418   via custom MATLAB code.

419   Measurements in the *y* direction were consistently larger than in the *x* direction,

420   especially in agarose (see Fig. 2bd). We believe this is due to a portion of the beam in

421   the y direction impinging on different media (water instead of agarose, or immersion oil

422   instead of glass, see Fig. 1b). The slight index mismatch may reduce the resolution of

423   the damage spot or its imaging. In agarose calculations, we set ω_0 in Eq. 2 equal to the

424   calculated ω_0 in the *x* direction (see Tab. 1). In glass calculations, the refractive indices

425 and calculated ω_0 are very similar, thus, we set ω_0 in Eq. 2 equal to the average of the

426 calculated ω_0.

C. elegans cultivation, immobilization, imaging: We followed established procedure

428 for *C. elegans* strains cultivation on agar plates[32] at 15 or 20 °C, animal immobilization

429 by sodium azide, and imaging[13]. After immobilization, animals were rotated to a desired

430 orientation[4] under a fluorescence stereomicroscope and then imaged under an inverted

431 microscope.

C. elegans strains: We used the following strains for this study: *dlk-1(ju476)I; ofIs1[lin-*

433 *15ab+; trx-1::gfp]IV* (for regeneration ablations), *tax-2(p691)I; ofIs1[lin-15ab+; trx-*

434 *1::gfp]IV* (for nuclear and dendrite ablations), and NG3146 *gmIs18[ceh-23::gfp; rol-6]X*

435 (for dendrite bundle ablations).

***In vivo* ablation:** We followed preoperative procedures established for laser ablation in

437 *C. elegans*[13,33]. Animals carried fluorescently-labeled neurons. We mounted young

438 adults onto agarose pads with sodium azide for immobilization. We followed established

439 procedures to sever neurites by ablating them with 35-nJ pulses for 0.2 s [4,13]. Neurites

440 are approximately 10 μm deep in the animal. To characterize the transverse resolution

441 of laser damage, we severed tightly-bundled fibers in the amphid dendrite bundle (Fig.

442 3a). We measured the gap between unsevered fibers using ImageJ. For characterizing

443 axial resolution, we aimed our laser at the ASJ nucleolus, which is 10-20 μm deep, and

444 ablated it with 50-nJ pulses for 15 s (Fig. 3b), following established protocol[13]. We also

445 ablated at defined locations above or below the dendrite (Fig. 3cd) and noted

446 percentage of successful severing.

447   **Regeneration characterization:** We followed procedures previously established in our

448   laboratory for studying regeneration[26]. In young adult animals we severed the axon, the

449   axon and ipsilateral dendrite, or the axon and then ablated 0.5 μm above or below the

450   ipsilateral dendrite without severing (Fig. 4ab). We followed postoperative procedures to

451   recover worms in nematode growth medium and continued cultivation at 20°C. We

452   reimaged worms 48 hours post-ablation and noted the frequency of regeneration.

453   **Statistics and interpretation of results:** We calculated *p*-values for frequency of

454   successful cuts and regeneration with Fisher's exact test.

Wang, *et al.*

Acknowledgements

References

1   Maiman, T. H. Stimulated Optical Radiation in Ruby. *Nature* **187**, 493-494 (1960).

2   Chung, S. H. & Mazur, E. Surgical applications of femtosecond lasers. *Journal of Biophotonics* **2**, 557-572 (2009).

3   Phipps, C. *Laser Ablation and its Applications*. Vol. 129 (2007).

4   Chung, S. H. & Mazur, E. Femtosecond laser ablation of neurons in C. elegans for behavioral studies. *Appl. Phys. A-Mater. Sci. Process.* **96**, 335-341, doi:10.1007/s00339-009-5201-7 (2009).

5   Hoy, C. L. *et al.* Clinical Ultrafast Laser Surgery: Recent Advances and Future Directions. *IEEE Journal of Selected Topics in Quantum Electronics* **20**, 242-255, doi:10.1109/JSTQE.2013.2287098 (2014).

6   Vogel, A. & Venugopalan, V. Mechanisms of pulsed laser ablation of biological tissues. *Chem. Rev.* **103**, 577-644 (2003).

7   Vogel, A., Noack, J., Huttman, G. & Paltauf, G. Mechanisms of femtosecond laser nanosurgery of cells and tissues. *Appl. Phys. B* **81**, 1015-1047 (2005).

8   Glezer, E. N. *et al.* Three-dimensional optical storage inside transparent materials. *Opt. Lett.* **21**, 2023-2025, doi:10.1364/OL.21.002023 (1996).

9   Schaffer, C. B., Brodeur, A., Garcia, A. F. & Mazur, E. Micromachining bulk glass by use of femtosecond laser pulses with nanojoule energy. *Opt. Lett.* **26**, 93-95 (2001).

10   Schaffer, C. B., Jamison, A. O. & Mazur, E. Morphology of femtosecond laser-induced structural changes in bulk transparent materials. *Appl. Phys. Lett.* **84**, 1441-1443, doi:10.1063/1.1650876 (2004).

484 11 Watanabe, W. & Itoh, K. Motion of bubble in solid by femtosecond laser pulses.
485   *Opt. Express* **10**, 603-608, doi:10.1364/OE.10.000603 (2002).

486 12 Saerchen, E. *et al.* Femtosecond laser induced step-like structures inside
487   transparent hydrogel due to laser induced threshold reduction. *PLOS ONE* **14**,
488   15, doi:10.1371/journal.pone.0222293 (2019).

489 13 Chung, S. H., Clark, D. A., Gabel, C. V., Mazur, E. & Samuel, A. D. The role of
490   the AFD neuron in C. elegans thermotaxis analyzed using femtosecond laser
491   ablation. *BMC Neurosci.* **7**, 30 (2006).

492 14 Harreguy, M. B. *et al.* Ytterbium-doped fibre femtosecond laser offers robust
493   operation with deep and precise microsurgery of C. elegans neurons. *Sci. Rep.*
494   **10**, 4545, doi:10.1038/s41598-020-61479-0 (2020).

495 15 Wang, Y. L., Grooms, N. W. F., Civale, S. C. & Chung, S. H. Confocal imaging
496   capacity on a widefield microscope using a spatial light modulator. *PLOS ONE*
497   **16**, e0244034, doi:10.1371/journal.pone.0244034 (2021).

498 16 Liu, J. M. Simple technique for measurements of pulsed Gaussian-beam spot
499   sizes. *Opt. Lett.* **7**, 196-198, doi:10.1364/OL.7.000196 (1982).

500 17 Yariv, A. *Optical Electronics in Modern Communications*. (Oxford University
501   Press, 1997).

502 18 Paschotta, R. *Field Guide to Laser Pulse Generation*. (Society of Photo Optical,
503   2008).

504 19 Evans, R., Camacho-López, S., Pérez-Gutiérrez, F. G. & Aguilar, G. Pump-probe
505   imaging of nanosecond laser-induced bubbles in agar gel. *Opt. Express* **16**,
506   7481-7492, doi:10.1364/OE.16.007481 (2008).

507 20 Perez-Gutierrez, F., Camacho-López, S. & Aguilar, G. Time-resolved study of the
508   mechanical response of tissue phantoms to nanosecond laser pulses. *J. Biomed.*
509   *Opt.* **16**, 115001 (2011).

510 21 Sung-Jin, P., Goodman, M. B. & Pruitt, B. L. (IEEE).

511 22 Fujiwara, E., Cabral, T. D., Sato, M., Oku, H. & Cordeiro, C. M. B. Agarose-
512   based structured optical fibre. *Sci. Rep.* **10**, 7035, doi:10.1038/s41598-020-
513   64103-3 (2020).

514 23 Xiong, R. & Sugioka, K. Improved 3D cellular morphometry of Caenorhabditis
515   elegans embryos using a refractive index matching medium. *PLOS ONE* **15**,
516   e0238955, doi:10.1371/journal.pone.0238955 (2020).

517 24 Chung, S. H., Schmalz, A., Ruiz, R. C. H., Gabel, C. V. & Mazur, E.
518   Femtosecond Laser Ablation Reveals Antagonistic Sensory and Neuroendocrine
519   Signaling that Underlie C-elegans Behavior and Development. *Cell Reports* **4**,
520   316-326, doi:10.1016/j.celrep.2013.06.027 (2013).

521 25 Hammarlund, M., Nix, P., Hauth, L., Jorgensen, E. M. & Bastiani, M. Axon
522   Regeneration Requires a Conserved MAP Kinase Pathway. *Science* **323**, 802-
523   806 (2009).

524 26 Chung, S. H. *et al.* Novel DLK-independent neuronal regeneration in
525   Caenorhabditis elegans shares links with activity-dependent ectopic outgrowth.
526   *Proc. Natl. Acad. Sci. USA* **113**, E2852-E2860, doi:10.1073/pnas.1600564113
527   (2016).

528 27 Stuart, B. C., Feit, M. D., Rubenchik, A. M., Shore, B. W. & Perry, M. D. Laser-
529   Induced Damage in Dielectrics with Nanosecond to Subpicosecond Pulses.
530   *Phys. Rev. Lett.* **74**, 2248-2251 (1995).

531 28 Lebugle, M., Sanner, N., Utéza, O. & Sentis, M. Guidelines for efficient direct
532   ablation of dielectrics with single femtosecond pulses. *Appl. Phys. A* **114**, 129-
533   142, doi:10.1007/s00339-013-8153-x (2014).

534 29 Boyd, R. W. in *Nonlinear Optics (Third Edition)* (ed Robert W. Boyd) 329-390
535   (Academic Press, 2008).

536 30 Gattass, R. R., Cerami, L. R. & Mazur, E. Micromachining of bulk glass with
537   bursts of femtosecond laser pulses at variable repetition rates. *Opt. Express* **14**,
538   5279-5284 (2006).

539 31 Niemz, M. H. *Laser-Tissue Interactions: Fundamentals and Applications*.
540   (Springer-Verlag, 2004).

541 32 Brenner, S. The genetics of Caenorhabditis elegans. *Genetics* **77**, 71-94 (1974).

542 33 Bargmann, C. I. & Avery, L. Laser killing of cells in Caenorhabditis elegans.
543   *Methods Cell Biol.* **48**, 225-250 (1995).

544

545

546

Wang, *et al.*

547
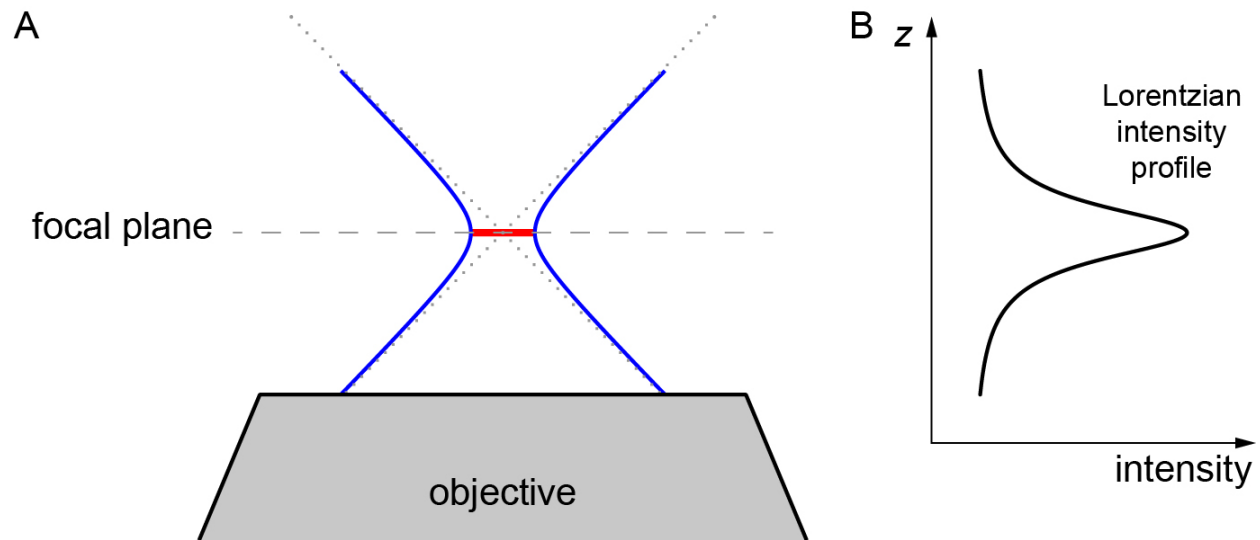
548 **S1 Fig. Focused beam profiles.** (A) Focused beams are hyperboloid in the axial

549 direction. Asymptotes indicated by dotted lines. Waist diameter indicated by red line on

550 focal plane (dashed line). (B) Corresponding intensity profile of beam shown in (A).